Cool skin signals observed from Advanced Along-Track Scanning Radiometer (AATSR) and *in situ* SST measurements

Haifeng Zhang[1,*], Alexander V. Babanin[1], Qingxiang Liu[1], Alexander Ignatov[2]

[1]*Department of Infrastructure Engineering, Melbourne School of Engineering, The University of Melbourne, Victoria 3010, Australia*

[2]*NOAA/STAR (Center for Satellite Applications and Research), College Park, MD 20740, USA*

[*]*Corresponding author: haifeng.zhang@unimelb.edu.au*

Abstract: Nighttime cool skin sea surface temperature (SST) signals, defined in this study as the differences between the SST_{skin} from the Advanced Along-Track Scanning Radiometer (AATSR) onboard Envisat satellite and *in situ* SSTs from drifting buoys and moorings, $\Delta T = SST_{skin}-SST_{insitu}$, are investigated on a global scale from July 2002 to April 2012. Global mean ΔT, averaged over the full study period, is -0.13 K, with most values falling between -0.1 and -0.2 K. The dominant role of wind speed on the ΔT is shown, with weaker winds usually corresponding to a cooler skin. The effect of air-sea temperature difference is also significant: warm skin ($\Delta T > 0$ K) can be observed under large positive air-sea temperature differences. Other geophysical variables, such as the total column water vapor, *in situ* SST, and net heat flux, also affect ΔT, but to a lesser degree. Significant increase of ΔT size with SST_{insitu} is observed when SST_{insitu} is > 28 °C. Tropical waters, such as the tropical Indian Ocean and the tropical warm pool (western Pacific and eastern Indian Ocean), are more frequently covered with a cool skin, largely due to the calm winds, very warm waters (especially for SST_{insitu} > 28 °C), and other environmental conditions supporting the development of large cool skin events. The ΔT seasonal pattern in the southern hemisphere is more regular, compared to the northern hemisphere. In both hemispheres, larger cool skin signals are seen during the local summer, mainly due to weaker winds. According to several previous cool skin models, higher winds tend to result in thinner cool skin layer depths, and hence in smaller ΔT amplitudes, regardless of stronger evaporation and heat loss. Given that wind is closely coupled with waves and turbulent mixing with wave breaking, the dependencies of ΔT on a few wave parameters are also investigated. A strong (moderate) dependency of ΔT on wave height (wave steepness) is identified, while the dependency of ΔT on wave breaking probability is less discernible.

Key words: sea surface temperature, cool skin, AATSR, seasonal patterns, wave breaking.

1. Introduction

It has been long known that the skin sea surface temperature (SST) is usually slightly cooler than the temperature immediately below, referred to as the cool skin effect or "skin effect", for short (e.g., Woodcock, 1941, 1947). According to the Group for High Resolution SST (GHRSST; Donlon et al., 2007) practical definitions, the skin SST refers to the temperature at around 10-20 μm depth, measured by an infrared (IR) radiometer typically operating at 3.7-12 μm wavelengths. Conductive diffusion is dominant in this layer. Cool skin exists because of the combined cooling effects of the longwave radiation and the latent and sensible heat fluxes (e.g., Saunders, 1967; Fairall et al., 1996). Since under most circumstances the net heat flux is from the ocean to the atmosphere, the cool skin is usually present with an amplitude of a few tenths of a degree. In the daytime, when the wind is calm and solar insolation strong, diurnal warming can have amplitudes of several Kelvins, which may offset the cool skin effect (e.g., Fairall et al., 1996; Gentemann et al., 2003). Diurnal warm layer tends to vanish at night, when a near constant temperature profile is restored in the upper few meters up to the bottom of the skin layer, which is referred to as the subskin SST, $SST_{subskin}$, measured by a microwave (MW) sensor at ~ 1 mm depth. Incorporating a diurnal warm and cool skin layers' schemes in a numerical weather prediction or a climate model has been shown to improve the model's accuracy, due to more accurate estimation of air-sea interactions (e.g., Robertson and Watson, 1992; Zeng and Beljaars, 2005; Brunke et al., 2008; Masson et al., 2012; Clayson & Bogdanoff, 2013; Akella et al., 2017).

Numerous studies have been conducted to observe and/or model the cool skin layer (e.g., Saunders, 1967; Hasse, 1971; Brutsaert, 1975; Liu et al., 1979; Hepplewhite, 1989; Schlüssel et al., 1990; Soloviev and Schlüssel, 1994, 1996; Fairall et al., 1996; Wick et al., 1996; Wick and Jessup, 1998; Artale et al., 2002; Donlon et al., 2002; Castro et al., 2003; Minnett, 2003; Tu and Tsuang, 2005; Ward, 2006; Minnett et al., 2011; Alappattu et al., 2017). Most of these studies used shipborne IR skin SSTs and coincident depth SSTs at a few centimetres to metres depths. The spatial and temporal scales are therefore restricted to the ships' duration and routes. While some studies used both daytime and nighttime data (e.g., Kent et al., 1996; Minnett, 2003; Minnett et al., 2011), it is not uncommon for some authors to adopt nighttime data only, to minimize the complication caused by diurnal warming (e.g., Horrocks et al., 2003). With data of high accuracy but sometimes limited in amount, a series of physical or empirical cool skin models have been developed, which can be generally divided into two groups. The first group, represented by the model proposed in Saunders (1967), considers two essential mechanisms controlling the heat fluxes across the molecular skin layer: free convection, caused by the thermal instability, and the salinity gradient across the cool skin itself under very calm winds (< 2 m s^{-1}), and forced convection driven by the surface shear stress. Many studies followed with foci on determining the Saunders' proportionality constant λ and then the thickness of the cool skin layer (e.g., Paulson and Simpson, 1981; Robinson et al., 1984; Wu, 1985; Fairall et al., 1996; Artale et al., 2002; Tu and Tsuang, 2005). The other group of parameterizations was developed based on the surface renewal theory, which assumes that a part of the surface layer is removed and replaced by water from beneath (e.g., Brutsaert, 1975; Liu et al., 1979; Schlüssel et al., 1990; Soloviev and Schlüssel, 1994; Wick et al., 1996; Castro et al., 2003). In addition to the physical models, empirical parameterizations have been also proposed in more recent studies, relating the cool skin layer amplitude to environmental variables such as wind speed (e.g., Donlon et al., 2002; Minnett et al., 2011; Alappattu et al., 2017). Different models have been intercompared with each other in several studies (e.g., Kent et al., 1996; Castro et al., 2003; Horrocks et al., 2003; Tu and Tsuang, 2005).

Although spaceborne radiometers have been retrieving the skin SST on a global scale for almost four decades since early 1980s, satellite data have been scarcely used in cool skin investigation, likely due to several reasons. First, satellite IR and *in situ* SSTs represent waters of spatially and temporally different scales. Infrared SSTs are almost instantaneous area averages, whereas *in situ* SSTs are point data, which may be measured either instantaneously or averaged in time. Such systematic differences exist regardless of the sizes of the temporal and spatial windows employed in their collocation. Second, traditionally, the uncertainties in IR SST retrievals are considered too large (with a typical standard deviation, SD ~ 0.5 K, when validated against drifting or mooring buoy measurements), making it challenging to analyse the cool skin signal, whose amplitude is typically much smaller. Several factors contribute to this large uncertainty, related to the instrument (spectral response, radiometric noise, in-flight calibration, etc.) and retrieval algorithms (including cloud screening, aerosol detection, correction for the effects of water vapor absorption, etc.) (e.g., Kilpatrick et al., 2015).

These issues have been presumably minimized in the (Advanced) Along Track Scanning Radiometers, (A)ATSRs, SST_{skin} data sets produced by the (A)ATSR Reprocessing for Climate (ARC) project. The (A)ATSRs are characterized by more accurate in-flight calibration and dual-view technique, which in turn offer an improved potential for accurate atmospheric correction (Llewellyn-Jones et al., 2001). In particular, the ARC project retrieves SST_{skin} using coefficients based on radiative transfer models (RTM), independently of *in situ* measurements. Recall that many operational SST retrieval algorithms are empirically regressed against *in situ* measurements, and therefore may not be fully independent from those. Although not without its own limitations, the ARC SST_{skin} data may be thus better suited for skin effect studies (Murray et al., 2000; see more detail in section 2.1 and 3).

This paper characterizes the cool skin behaviours on a global scale, using nearly ten-year nighttime AATSR SST_{skin} data, in conjunction with collocated in situ SSTs, measured by drifting, coastal and tropical mooring buoys. The structure of the paper is as follows. Section

2 introduces the data sets and methods. Section 3 briefly describes AATSR and *in situ* data. Section 4 characterizes the cool skin signals, including their statistics and relationships with different environmental variables. Discussion and conclusions are presented in sections 5 and 6, respectively.

2. Data and Methods

2.1. Data sets

2.1.1 AATSR SST_{skin} data

The AATSR sensor was flown onboard ESA's Envisat satellite, launched in March 2002 as a successor to ATSRs -1 and -2 (launched in July 1991 and April 1995, respectively). Compared to previous missions, several improvements have been made to this family of instruments, including: 1) the dual-view (nadir and forward views ~ 55° from zenith) geometry, within a few minutes of each other, allowing for more effective atmospheric correction; 2) a rigorous pre-launch calibration programme and continuous onboard calibration of the thermal channels against two stable, high-accuracy black-body calibration targets; and 3) the high clarity and sensitivity of the IR image data, mainly due to the special mechanical coolers, which were used for the first time on ATSR-1 (Llewellyn-Jones et al., 2001; Llewellyn-Jones and Remedios, 2012). In addition, from the very onset it was intended that ATSR SSTs should be obtained independently of *in situ* measurements, through the use of RTM to define ATSR retrieval coefficients (Zàvody et al., 1995; Merchant et al., 1999; Embury and Merchant, 2012; Embury et al., 2012a; Embury et al., 2012b).

The Envisat crosses the equator at ~ 10 am/pm local time. At night, SST_{skin} is retrieved using bands centred at 3.7, 11, and 12 μm. During the daytime, channel at 3.7 μm is not used, due to solar reflectance and scattering. There are up to four retrieved SSTs in each pixel, referred to as N2 (nadir two channel), N3 (nadir three channel), D2 (dual-view two channel) and D3 (dual-view three channel), respectively.

The data used in this study, are from the latest third AATSR reprocessing, level 2 pre-collocation (L2P) dataset, spanning more than nine years from late July 2002 to early April 2012 (accessed from ftp://ats-ftp-ds.eo.esa.int). The third reprocessing products use the same algorithm as the ARC v1.1 data, with the only difference being that the former is GHRSST format compliant while the latter is not (O. Embury, personal communication). Skin SSTs without sensor-specific error statistics bias (SSES Bias) correction are used. To avoid possible complication caused by diurnal warming, and inconsistent day/night bands and algorithms, only highest quality (quality level, QL = 5) nighttime D3 data are selected. According to prior studies, D3 retrievals are considered the most accurate (e.g., Embury et al., 2012a; Merchant et al., 2012).

2.2.2 In Situ SST measurements

It is known that strong diurnal warming events could persist well into the late night or even the next early morning, especially under very calm conditions (e.g., Gentemann et al., 2003; Gentemann and Minnett, 2008; Zhang et al., 2018). It is extremely challenging to totally exclude the diurnal warming residuals in the upper layer. In this study, it is even more so as the AATSR has an early night local passing time of ~ 10 pm. Nonetheless, previous studies have shown that the diurnal warming residuals in the upper few meters can be minimum under well-mixed conditions, i.e. wind speed > 2 m s^{-1} at night (e.g., Donlon et al., 2002; Matthews et al., 2014; Zhang et al., 2016). Hence, SST measurements from *in situ* platforms such as drifting buoys at ~ 20 cm depth, and tropical and coastal moorings at ~ 1 m depth, are expected to well represent $SST_{subskin}$. In this study, *in situ* SST data are obtained from NOAA *in situ* SST Quality Monitor version 2 (*i*Quam 2; www.star.nesdis.noaa.gov/sod/sst/iquam/)

system (Xu and Ignatov, 2014). Only data of drifting, tropical and coastal moored buoys are used.

In addition to applying the appended QL filter, we also looked at the SSTs as a function of latitude. In every 2° latitudinal band, any value falling outside of the mean ± 2×SD range, was discarded. Enlarging the window to 3×SD increased the data counts by only 2.3%, while introducing more noise, and therefore was not adopted. In addition, *in situ* SSTs < -5 °C are considered unrealistic and also excluded.

2.2.3. Environmental variables

All meteorological variables in this study are obtained from the daily European Centre for Medium-Range Weather Forecasts (ECMWF) interim reanalysis (ERAI; Dee et al., 2011), namely the 10 m wind speed (U_{10}), air temperature (T_a), latent heat flux (Q_l), sensible heat flux (Q_s), net longwave thermal radiation (Q_{lw}), and total column water vapour (TCWV). The spatial resolution is by default 0.75° and temporal resolution 3-hrs. For instantaneous variables like U_{10}, T_a, and TCWV, analysis and forecast data are combined: analysis for every 6 hours (00:00, 06:00, 12:00, 18:00 UTC) and forecast for the hours in between (03:00, 09:00, 15:00, 21:00), while all the heat fluxes are forecast data only. At night, when there is no solar insolation, the net heat flux Q_{net} is calculated as the sum of $Q_l + Q_s + Q_{lw}$, with negative sign indicating heat from the ocean to the atmosphere, and positive the other way around.

The ERAI products are among the most widely used reanalysis data sets, thanks to their good quality. The ERAI environmental variables used in this study have been extensively validated against satellite and *in situ* measurements, and inter-compared with other reanalysis data sets (e.g., Brunke et al., 2011; Chaudhuri et al., 2013). For instance, Brunke et al. (2011) found that the ERAI latent heat flux and wind stress fields perform very well when evaluated against direct covariance latent heat flux and inertial-dissipation wind stresses measured from cruises in the tropics, as well as in the mid- and high latitudes. For more detail of the validation and quality of the ERAI meteorological fields, refer to Dee et al. (2011), Brunke et al. (2011), and Chaudhuri et al. (2013) and references therein.

2.2. Collocation and quality control

The QL = 5 AATSR and QC'd *in situ* SST data are first collocated. The temporal and spatial windows are set to 1 hr and 0.1°, respectively, comparable to (or more conservative than) in other similar studies, which use 3 hr and 10 arc min thresholds (e.g., O'Carroll et al., 2008; Xu and Ignatov, 2016). Any AATSR and *in situ* collocations with absolute difference > 10 K are discarded. Then, meteorological variables at the nearest ERAI pixel are assigned to each collocation, meaning that the temporal and spatial windows are half of the ERAI's resolutions: 1.5 hrs and 0.375°. At 10 ± 1.5 pm local time in high latitudes, there may still be positive downward solar insolation, especially in summer. These data, accounting for ~4.3% of all collocations, have been discarded. Finally, the resulting match-up data set includes total N = 594,777 collocations.

3. Quality of AATSR and *in situ* SSTs

The high quality of AATSR SSTs have been illustrated in a number of studies (e.g., Corlett et al., 2006; Noyes et al., 2006; O'Carroll et al., 2006; O'Carroll et al., 2008; Reynolds et al., 2010; Kennedy et al., 2012; Merchant et al., 2012; Merchant et al., 2014; Xu and Ignatov, 2016). Several publications used a triple collocation method (TCM) and showed that AATSR SSTs are as precise as *in situ* observations, or better. For instance, O'Carroll et al. (2008) showed that the spatially averaged nighttime AATSR D3 bulk SST observations (converted using the Fairall et al. 1996 model) for 2003 have a SD ~ 0.16 K vs. drifters' SD ~ 0.23 K. Merchant et al. (2012) found the ARC SSTs have a SD ~ 0.14 K during 2003 to 2009, compared to SD ~ 0.15-0.18 K for drifters. Merchant et al. (2014, their Table 2) described the

ARC v1.1 data set as the "most accurate and stable SST product available" in comparison with several other data sets. In terms of accuracy, although meeting the < 0.1 K requirement, some authors did observe a small warm bias of ~ 0.04-0.06 K when comparing nighttime AATSR data against drifting buoys or radiometers (e.g., Corlett et al., 2006; Noyes et al., 2006).

Note that the ARC skin SST data may be also subject to their own limitations. Just like any IR sensor, there is no SST_{skin} retrieved when and where cloud is present. Compared to empirical regression algorithms, an RTM-based retrieval scheme employs numerous environmental data sources (e.g., various atmospheric components, atmospheric and marine aerosols), all of which could contribute to the SST uncertainty to a different extent (Embury et al., 2012b). The RTM may not be fully accurate, either. In addition, the sensitivity of SST retrievals to water vapor or to actual SSTs may vary across different regions (Embury and Merchant, 2012). However, at this moment, this remote sensing skin SST data set is thought to be the most suitable for a global, long-term skin effect study (Merchant et al., 2014).

Xu and Ignatov (2016) estimated SDs for tropical and coastal moorings as 0.17 K and 0.40 K, respectively. To employ as much data as possible, mooring measurements are also retained in this study, and validation statistics are not stratified by *in situ* data types.

4. Results

4.1. General statistics

The overall statistics of AATSR satellite SST_{skin} minus SST_{insitu} are shown in Fig. 1. The mean ΔT (defined as $SST_{skin} - SST_{insitu}$) is -0.13 K, which is comparable to the findings in previous studies such as Donlon et al. (2002) and Minnett et al. (2011). The 0.46 K SD is obviously larger than the SDs of ~ 0.16 or 0.14 K in O'Carroll et al. (2008) and Merchant et al. (2012), which were based on a TCM, which accounts for the uncertainties in SST_{insitu}. The

RSD (robust SD, calculated as 1.5 times the median absolute deviation from the median) of 0.20 K is much smaller, since RSD is less sensitive to outliers. Fig. 1b shows the distribution of ΔT. The peak is found between -0.2 K and -0.1 K, with 21.4% of data falling in this range. The spread of the ΔT values is similar to the studies which used shipborne IR skin SST (e.g., Hepplewhite et al., 1989; Donlon and Robinson, 1997), except that in this study, the positive ΔT values form a larger portion (25.6%). These positive ΔT values could be due to many reasons: residual diurnal warming, satellite and *in situ* data noises, real warm skin signals, etc. However, the subsequent analyses will show that a large part of those make physical sense and may be explained by the corresponding environmental conditions.

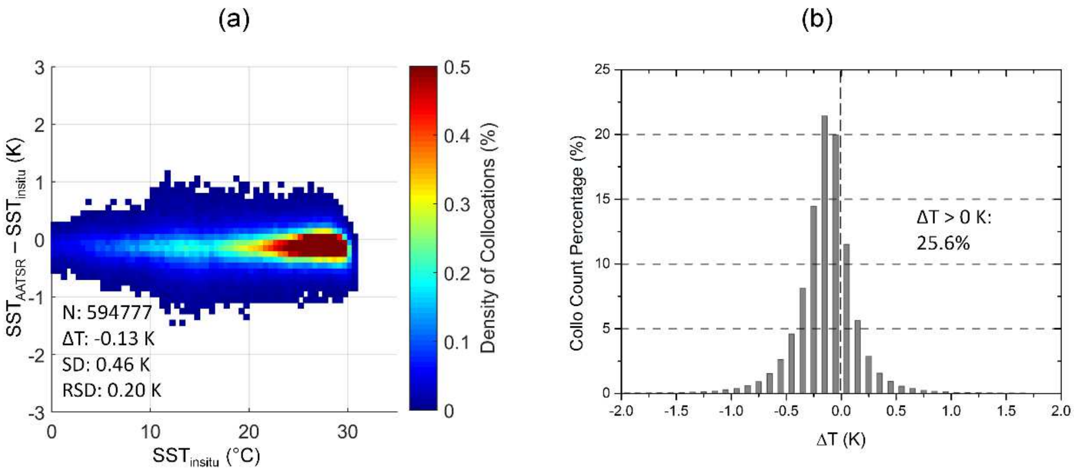

Fig. 1. (a) Density of collocations as a function of SST_{insitu}, with overall statistics of ΔT (= SST_{skin} - SST_{insitu}) superimposed. (b) Frequency distribution of ΔTs.

The spatial and temporal distributions of the collocations are shown in Fig. 2. The most populated regions are in the low-to-mid latitudes of the Northern Atlantic (Fig. 2a). The collocations in the Tropical Pacific are also abundant. Fewer collocations are found for some areas, particularly in the high latitudes (> 40°N/S), largely due to the lack of *in situ* measurements, and over the eastern Indian Ocean and the tropical warm pool (TWP; tropical eastern Indian Ocean and western Pacific Ocean) areas, due to a combination of frequent clouds and sparse *in situ* data. Fig. 2b shows that the number of collocations in both hemispheres has increased with time, as more *in situ* measurements became available. There are nearly always more collocations in the northern hemisphere than in the southern hemisphere.

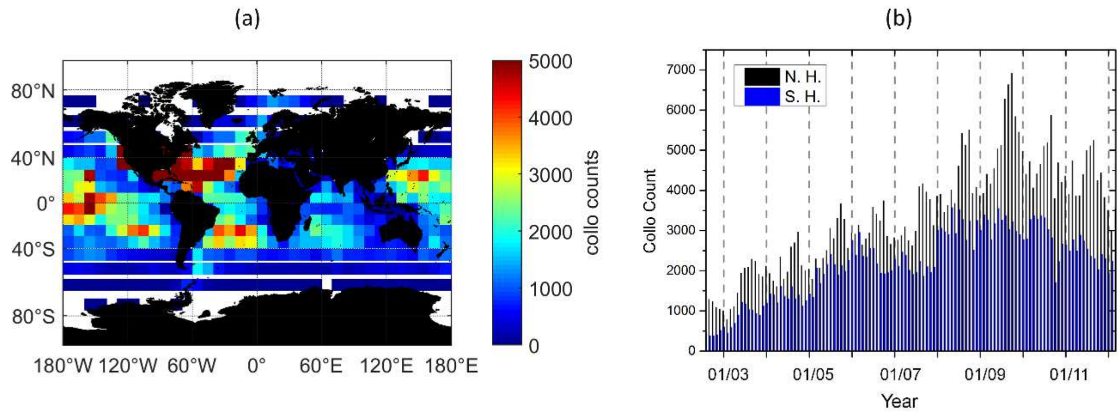

Fig. 2. (a) Spatial distribution of the collocations. Bin size is 10°×10°. (b) Monthly collocation counts in the northern (black bars) and southern (blue bars) hemispheres.

4.2. Dependencies of ΔT on environmental variables

The effects of different meteorological factors on ΔT have been investigated, including U_{10}, air-sea temperature difference T_a-T_s (here T_s is SST_{insitu}), TCWV, SST_{insitu}, Q_{net} and its components. Here, QC'd *i*Quam SST_{insitu} observations are chosen to represent T_s over the ERAI SST reanalysis product. From Table 1 in Dee et al. (2011), since February 2009, the SST field used in ERAI comes from the Operational Sea Surface Temperature and Sea-Ice Analysis (OSTIA), a foundation SST product incorporating multiple SST sources, including ship measurements obtained at a significantly deeper layer than buoys (Donlon et al., 2012). Traditional ship SSTs, with typically less accurate depth information, are considered less reliable than buoys (Zhang et al., 2009). Therefore, to adopt the most reliable data and to keep analyses consistent with the calculation of the ΔTs, QC'd *i*Quam buoy SST observations are used here.

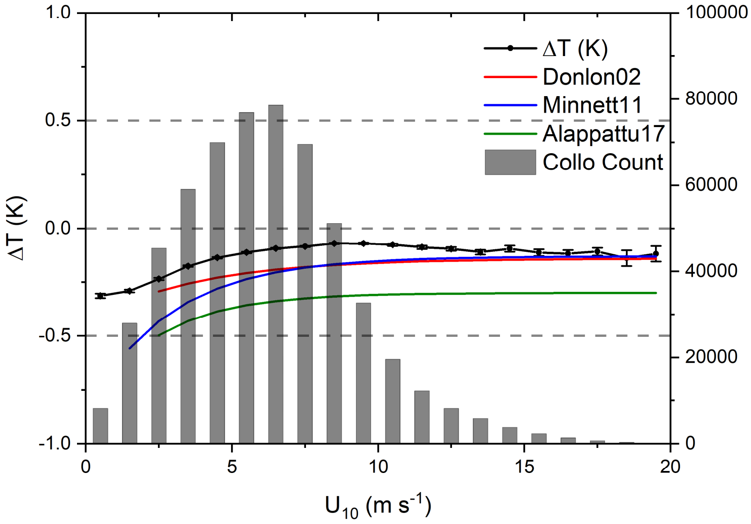

Fig. 3. Solid circles/Black line: dependencies of ΔT on U_{10}. The error bar is the 95% confidence level margin of error (MoE), i.e. 1.96 times the SD divided by the square root of the collocation number. The column bars indicate the collocation counts falling within each 1 m s^{-1} U_{10} interval. The red, blue, and green lines have been calculated using the Donlon et al. (2002), Minnett et al. (2011), and Alappattu et al., (2017) empirical parameterizations, respectively.

The cool skin amplitudes have been long known to strongly depend on U_{10}, as also shown in Fig. 3. The effect of wind on the cool skin amplitudes is twofold: through turbulent mixing and net heat flux. Increased winds result in stronger turbulent mixing, which reduces ΔT; while larger winds also typically lead to more net heat flux, which is expected to increase ΔT size. The combined effects of U_{10} and Q_{net} will be discussed later. When the wind is very calm (< 2 m s^{-1} in Fig. 3), the ΔTs have largest amplitudes, with mean values reaching -0.30 K to -0.35 K. As winds get stronger, ΔT climbs up steadily until U_{10} reaches 8-10 m s^{-1}, when ΔT starts to level off at -0.09 K to -0.12 K. The trend is very similar to observations made in previous studies, such as Donlon et al. (2002; hereafter D02), Minnett et al. (2011; hereafter M11), and Alappattu et al. (2017; hereafter A17), which are also plotted in Fig. 3. The empirical equations relating ΔT to wind speed are: $\Delta T = -0.14 - 0.30*\exp(-0.27*U_{10})$ in D02;

$\Delta T = -0.13 - 0.724*\exp(-0.35*U_{10})$ in M11; and $\Delta T = -0.30 - 0.55*\exp(-0.41*U_{10})$ in A17, respectively. Note that the ΔT range observed in this study, differs from the ones predicted by the models (which also all differ, as defined by the pre-exponent coefficient in the three formulations). The cool skin values reported here are smaller in size than D02 and M11 by 0.05-0.07 K for U_{10} between 4-12 m s^{-1} conditions. Model M11 predicts the largest ΔTs < -0.5 K at very calm winds (< 2 m s^{-1}). The line obtained in this study, and the D02 and M11, all tend to asymptotically converge at high winds (U_{10} > 13 m s^{-1}). The A17 model estimates significantly larger cool skin sizes for all wind conditions.

Several reasons might account for the ΔT difference between this study and the empirical equations, which all may contain uncertainties of different kinds. In particular, the AATSR skin SSTs are averaged over a relatively large area, in comparison with near-point data of shipborne radiometers and thermistors. Also, the temporal collocation between AATSR SST_{skin} and SST_{insitu} is within one hour, compared to only a few seconds to minutes between shipborne radiometers and thermistors. Finally, there may be a small warm bias residual in the nighttime D3 AATSR data, as found in previous studies (e.g., Corlett et al., 2006; Noyes et al., 2006), although they were validating different versions of AATSR data (see section 3). Diurnal warming residuals could partially be responsible for the smaller ΔT range found in this study when U_{10} is < 2 m s^{-1}, although they are expected to be progressively less critical for U_{10} > 2 m s^{-1}. As to the large difference between the A17, on the one hand, and observations and other models; on the other, note that the A17 coefficients were determined from coastal observations, which may have been affected by river discharge (Alappattu et al., 2017). A plot similar to Fig. 3 is also found in Embury et al. (2012a; their Fig. 3) and Alappattu et al. (2017; their Fig. 14).

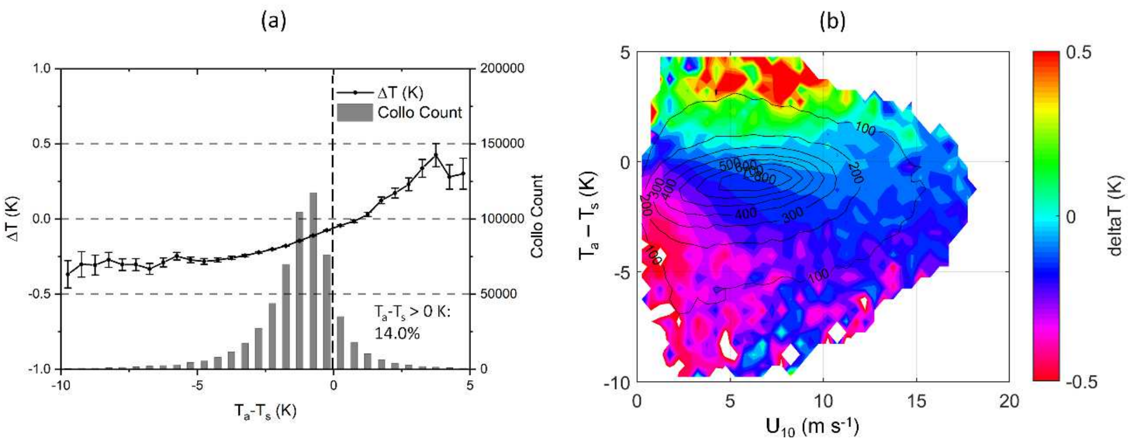

Fig. 4. (a) Dependency of ΔT on T_a-T_s (with the error bars at 95% confidence level margin of error, MoE). (b) Dependency of ΔT on T_a-T_s (binned into 0.5 K) and U_{10} (binned into 1 m s^{-1}). Black contour lines indicate the corresponding collocation counts in each 1 m s^{-1} × 0.5 K bin. Only bins with collocation counts >= 20 are plotted.

The effects of T_a-T_s on ΔT are shown in Fig. 4. Generally, when the air is cooler than the sea water, heat is lost from the sea to the air, thus favouring the cool skin development. Fig. 4a shows a steady climb of ΔT as T_a-T_s changes from negative to positive values, reaching ~ +0.4 K when the T_a-T_s is ~ 3-5 K. Since U_{10} is normally considered the most influential factor, the effect of T_a-T_s is further analysed stratified by U_{10} conditions, in Fig. 4b. As expected, the skin is coolest when the T_a-T_s reaches its minimal values, in conjunction with weakest winds. Increasing U_{10} reduces the cool skin amplitude, while increasing T_a-T_s is able to even reverse the sign of ΔT. For most conditions with positive T_a-T_s, ΔT is close to zero or slightly positive, and sharply increases along with T_a-T_s. It is noticed that very large positive T_a-T_s values typically occur for U_{10} < 10 m s^{-1} conditions. Also, Fig. 4a indicates that positive T_a-T_s values make up 14.0% of all data, which could explain at least a part of the 25.6% warm skin values in Fig. 1b.

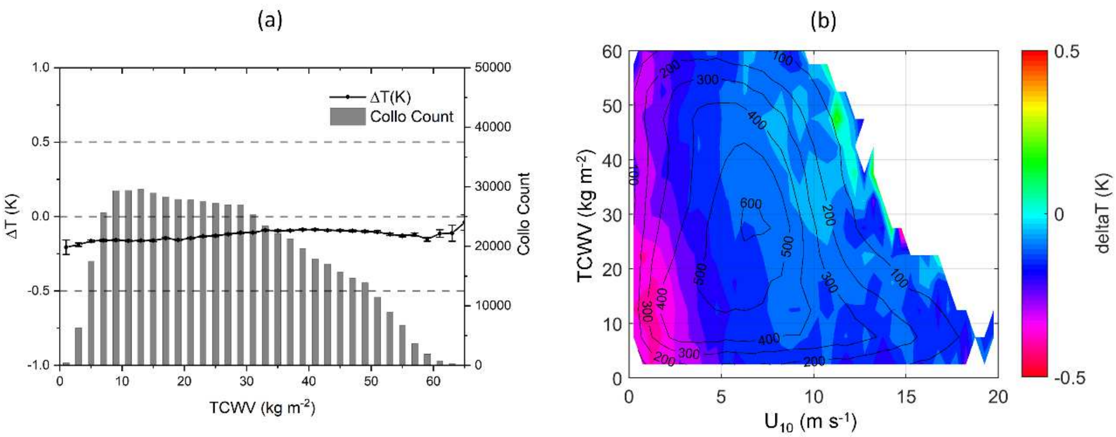

Fig. 5. Same as in Fig. 4 but for the dependency of ΔT on TCWV (binned into 5 kg m^{-2}).

The dependency of ΔT on TCWV is shown in Fig. 5. The TCWV variable is selected because the IR SST_{skin} retrievals mostly aim to correct for its effect as a part of the atmospheric correction algorithms, and therefore may reveal some residual sensitivity to it. Moreover, the TCWV field affects the value of the Q_l. According to Embury and Merchant (2012), the retrieval scheme of the AATSR data used in this study adopts coefficients banded by TCWV. The independence of the D3 retrievals on TCWV was illustrated by the near-zero biases over the whole TCWV range (Embury and Merchant, 2012; their Fig. 7d). In Fig. 5a, ΔT shows a weak upward trend when the TCWV increases from low (~ 5 kg m^{-2}) to middle range (~ 40 kg m^{-2}), but the change of ΔT is small (~ 0.11 K). From ~ 40 kg m^{-2} to higher TCWV, the ΔT levels off. When holding U_{10} fixed (Fig. 5b), increasing TCWV can slightly reduce the amplitude of ΔT. The largest ΔTs appear when the TCWV is low and U_{10} weak. Overall, the change of ΔT in the full range of the TCWV, under a certain U_{10} conditions, is relatively minor, except maybe for U_{10} > 8 m s^{-1}. Near-zero cool skin amplitudes are observed when U_{10} is strong (~ 12 m s^{-1}) and TCWV high (~ 50 kg m^{-2}).

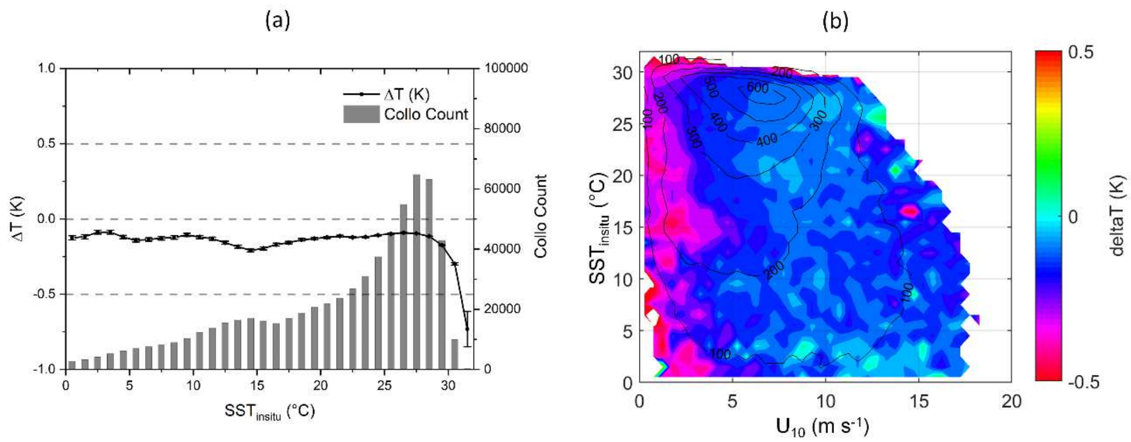

Fig. 6. Same as Fig. 4 but for the dependency of ΔT on SST_{insitu} (binned into 1 °C).

In Minnett et al. (2011), a possible temperature dependence of ΔT was reported (ΔT size increases as bulk SST changes from ~ 10 °C to ~ 18 °C when U_{10} < 3 m s^{-1}), although no robust conclusions were drawn due to the small match-up dataset. Here in Fig. 6a, we do not see a clear dependency of ΔT for SST_{insitu} < 28 °C. However, when SST_{insitu} is > 28 °C (especially > 30 °C), a sharp drop in ΔT is observed. The validation in Embury et al. (2012a) indicates little dependency of AATSR D3 SST_{skin} on latitudes, i.e. SST conditions. For fixed U_{10} in Fig. 6b, there is only little change with SST_{insitu} (except large ΔT amplitudes are seen for SST_{insitu} > 30 °C). Such warm waters basically only exist in the TWP area under very calm conditions (U_{10} < 3 m s^{-1}). We will investigate the TWP region in more detail in the next subsection.

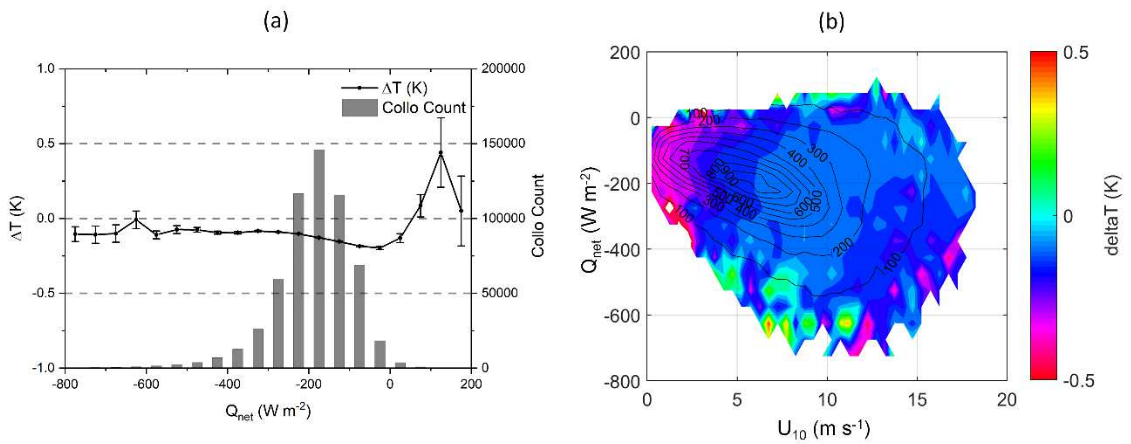

Fig. 7. Same as Fig. 4 but for the dependency of ΔT on Q_{net} (binned into 50 W m^{-2}).

The effects of Q_{net} on ΔT are complicated by its further coupling with other meteorological conditions, especially with U_{10}. In Fig. 7a, the ΔT dependency on Q_{net} does not show a clear trend for Q_{net} values < -400 W m^{-2}. A downward trend of ΔT is found for the most frequent Q_{net} values (from -350 to 0 W m^{-2}). This negative relationship is seemingly going against one's expectation of larger Q_{net} leading to larger ΔT amplitude. When plotting Q_{net} together with its accompanying U_{10}, it is noticed that, to a large extent, Q_{net} is determined by U_{10}: strong winds result in larger Q_{net} (Fig. 7b). Mixing induced by strong winds has dominated over the increased Q_{net}, preventing the establishment of large cool skins. This may be the main reason for the downward trend in Fig. 7a. In Fig. 7b, when U_{10} is determined, ΔTs are rather stable regardless of Q_{net} sizes, indicating the weaker role of Q_{net} in ΔT development. The positive ΔT peak for U_{10} between 5-10 m s^{-1} and Q_{net} between -400 and -600 W m^{-2}, as unexpected. This signal may be partially due to the sparse collocations under such conditions. It is interesting to note that when Q_{net} is positive, i.e. heat flux is going into the ocean, a sharp upward climbing of ΔT to positive values is seen (Fig. 7a). This makes physical sense in the authors' opinion. In Fig. 7b, we get more near zero and positive ΔT values under the rare positive Q_{net} conditions.

The ΔT dependencies on Q_l and Q_s largely follow those of Q_{net} and T_a-T_s, therefore not shown here. Q_{lw} has similar effects as Q_{net} on ΔT, but with a smaller amplitude, and also not shown.

Table 1 shows the statistics of the environmental variables for non-negative ΔTs and SST_{insitu} > 30 °C situations. Compared to the overall and negative ΔT statistics, non-negative ΔTs correspond to stronger winds and smaller T_a-T_s sizes. This is reasonable since higher U_{10} and smaller air-sea temperature differences both contribute to the development of a near-zero or positive ΔT. In Fig. 6a, we observe a sharp drop in ΔT for SST_{insitu} > 30 °C conditions. Such warm waters are normally only located in the tropical areas, especially in the TWP region. The far lower winds and larger negative T_a-T_s should account for the increased ΔT size. According to the validation in Embury et al. (2012a; their Fig. 12), AATSR D3 satellite data over these regions continue to show < 0.1 K biases. Embury and Merchant (2012) showed that the sensitivity of ARC AATSR D3 SSTs to actual SST is between 0.99 to 1.01 over the tropical region (their Fig. 14d), and a 10% increase in TCWV causes only a ~0.015 K decrease in the retrieved SST (their Fig. 13d; see also section 4.3 below).

Table 1. Statistics for non-negative ΔT and SST_{insitu} > 30 °C conditions. The overall and negative ΔT rows are for comparison.

	Collocation Counts	Mean ΔT (K)	Mean U_{10} (m s^{-1})	Mean T_a-T_s (K)	Mean TCWV (kg m^{-2})	Mean Q_{net} (W m^{-2})
Overall	594,777 (100%)	-0.13	6.20	-1.27	26.32	-187.54
ΔT < 0 K	442,657 (74.6%)	-0.27	6.00	-1.41	26.35	-186.59
ΔT >= 0 K	152,120 (25.4%)	0.27	6.77	-0.86	26.25	-190.31
SST_{insitu} > 30 °C	8,331 (1.4%)	-0.36	3.39	-1.90	47.34	-179.57

4.3. Spatial distribution of ΔT

In the previous subsection, we have shown that the major factors regulating ΔT are U_{10} and T_a-T_s. TCWV and Q_{net} play relatively minor roles. SST_{insitu} only has a significant impact when > 28 °C. In this subsection, we investigate the relationship between ΔT and all the variables by analysing their spatial distributions.

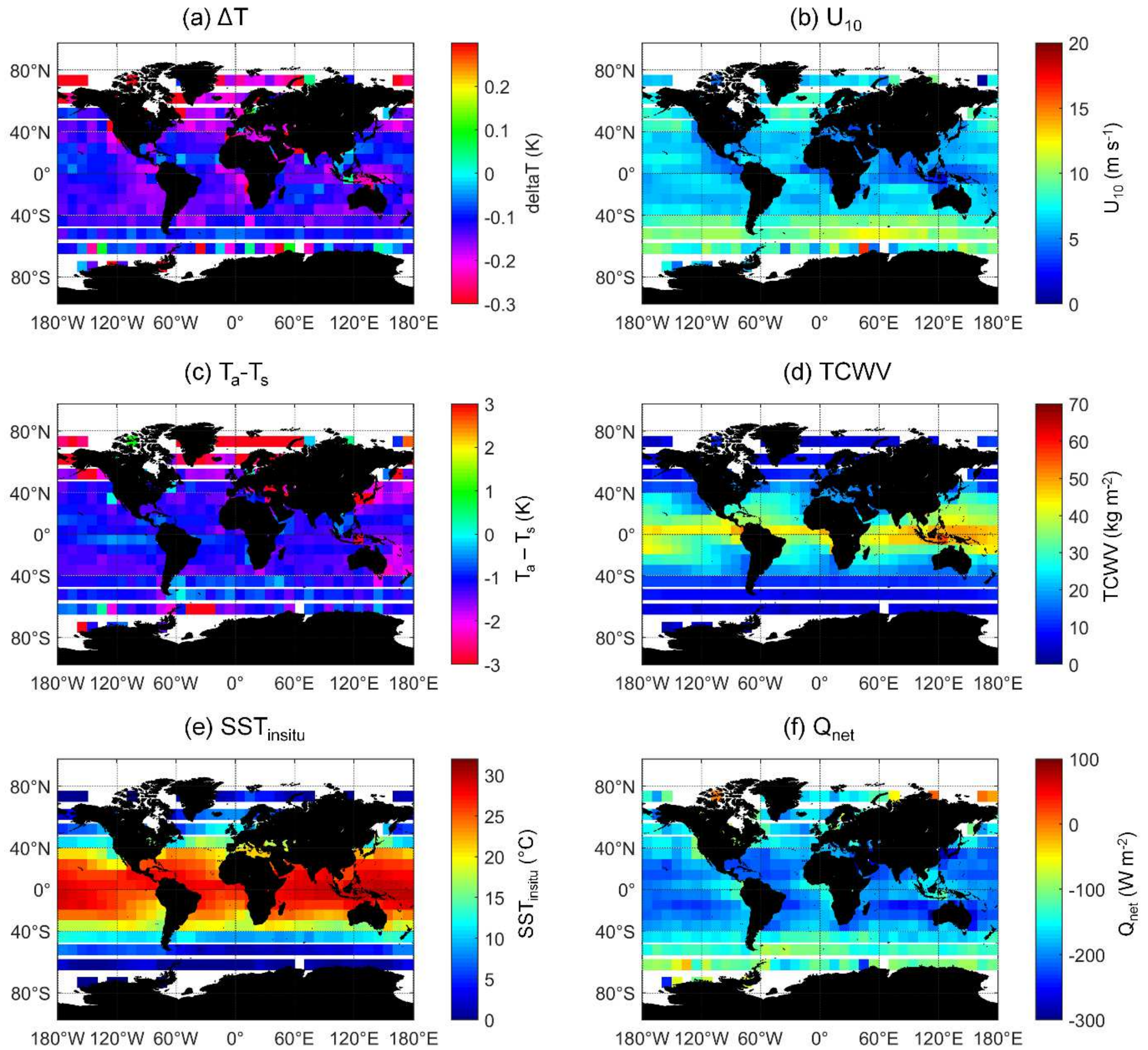

Fig. 8. Spatial distributions of (a) ΔT; (b) U_{10}; (c) T_a-T_s; (d) TCWV; (e) SST_{insitu}; and (f) Q_{net} averaged over the whole study period. Box size is 10° by 10°.

Fig. 8 shows the distribution of ΔT along with other environmental variables averaged over the study period within 10° by 10° boxes. Several features are quickly spotted. Over most of the global oceans, average ΔT is around -0.1 to -0.15 K. The distribution pattern of the ΔT closely follows that of U_{10}: low winds correspond to large ΔT sizes. However, it is also noticed that large ΔT over different regions can be caused by one or a combination of different factors. Several regions are selected as examples for illustration.

(1) Over the tropical areas, namely to the west of the Middle America, Gulf of Guinea, and the TWP region. These areas have nearly year-round low winds (< 5 m s^{-1}), largely responsible for a very cool skin.

(2) Over the west coast of Canada and the USA and to the west of Peru and Chile. Contributing factors to the large ΔT include the low winds (Fig. 8b) and low TCWV (Fig. 8d). The SST_{insitu} values are atypically low for their latitudes, due to the cold California and Peru Currents, respectively, which may also explain the low TCWV here.

(3) Over the Mediterranean Sea. Nearly all factors support large ΔT events: low winds, large negative air-sea temperature differences, and low TCWV.

(4) Over the high-latitude north Atlantic Oceans. Large ΔTs are observed due to the significantly cooler and dry air, even though U_{10} is relatively large.

The ΔT sizes are more irregular in the southern high latitudes, mainly due to the severe sparseness of collocations (see also Fig. 2a).

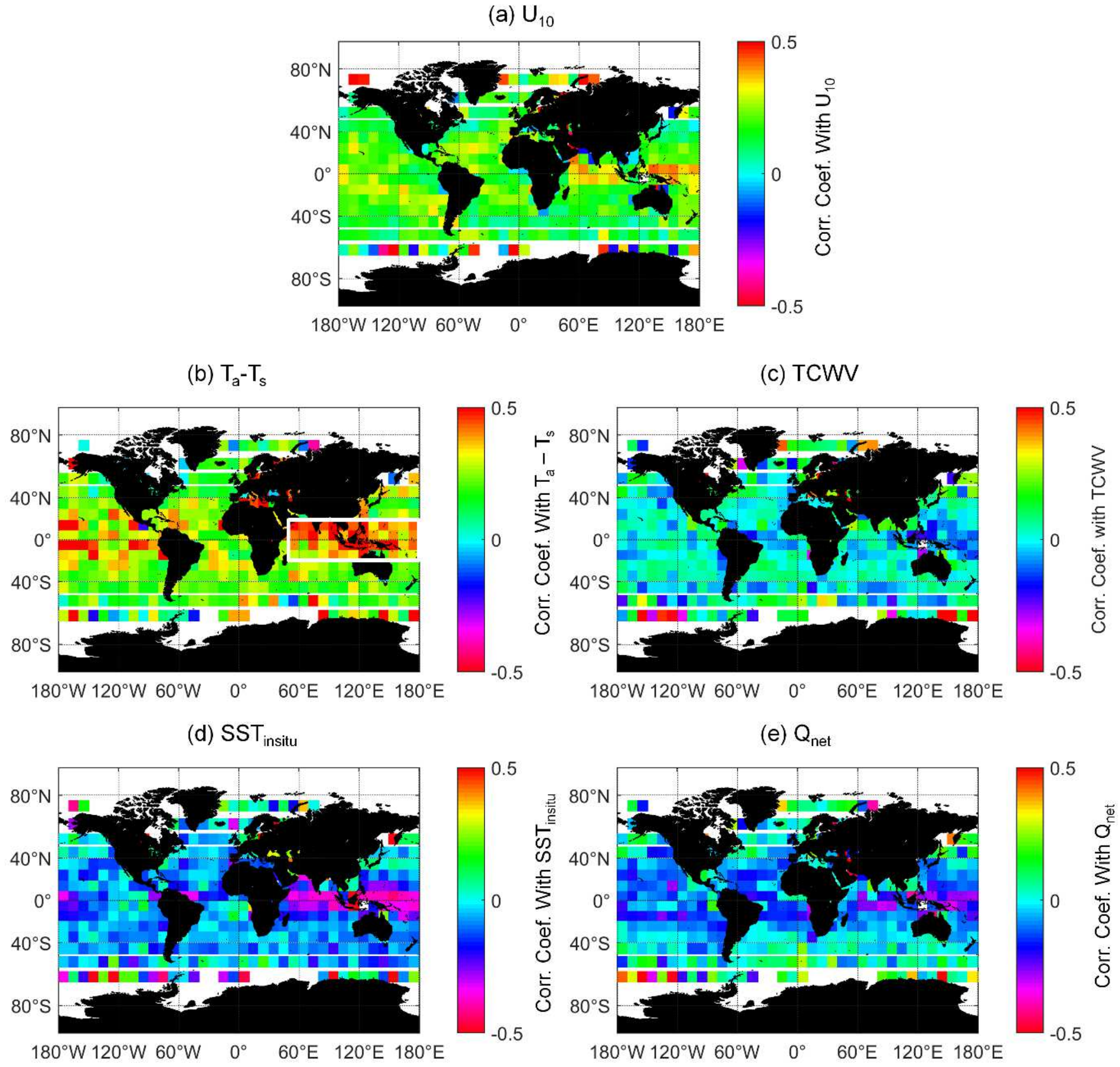

Fig. 9. Correlation coefficients between ΔT and (a) U_{10}; (b) T_a-T_s; (c) TCWV; (d) SST_{insitu}; and (e) Q_{net}. The white box in panel (b) is within (50°E-180°, 20°S-20°N). See text for further illustration.

Further to Fig. 8, we calculated the correlation coefficients (Rs) between ΔT and the environmental variables (Fig. 9). Overall, correlation coefficients are mostly mild (between -0.5 and 0.5) for all the variables, due to the complicated interactions and noise in the data. Positive correlations between ΔT and U_{10} and T_a-T_s are observed over most of the global oceans, as expected (Figs. 9a and b; when interpreting the correlations, please keep in mind that the majority of ΔT values are negative). Particularly large positive Rs (~ 0.5) are found over the tropics, including the TWP region, tropical Indian Oceans, and the waters adjacent to the Middle America (Figs. 9a and 9b). The Rs between TCWV and ΔT are mixed of near-zero positive and negative values, indicating TCWV's relatively weak influence (see also Fig. 5), except over the tropical Indian Ocean and the TWP region, where large negative Rs are found (Fig. 9c). The dependency of ΔT on SST_{insitu} is also weak, and not well defined over most of the oceans (Fig. 9d). However, large negative Rs are seen over the tropical Indian Ocean and TWP domain, consistent with the sharp drop of ΔT for SST_{insitu} > 28 °C in Fig. 6a. Over most of the low-to-mid latitude oceans, especially over the tropical Indian Ocean and TWP domain, Q_{net} has a negative effect on the ΔT development, confirming the finding in Fig. 7a.

The above results have highlighted the tropical Indian Ocean and the TWP domains, which motivates us to conduct a further regional analysis. The region selected is 50°E to 180°, 20°S to 20°N (see the white box in Fig. 9b). The change of ΔT with U_{10}, T_a-T_s, TCWV, and Q_{net}, is now stratified by SST_{insitu}. Focusing only on the SST_{insitu} > 28 °C conditions, we divided the SST_{insitu} values into six bands: < 28 °C, every half a degree from 28 °C to 30 °C, and > 30 °C. The results are displayed in Fig. 10. The size of ΔT quickly increases as SST_{insitu} warms up from 28 °C to 30 °C, in line with Fig. 6a. Wind speed drops from around 6.9 m s^{-1} for SST_{insitu} < 28 °C to ~ 3.3 m s^{-1} when SST_{insitu} is > 30 °C, and T_a-T_s reduces from -0.9 K to -1.9 K, both contributing to a cooler skin. The negative correlation between ΔT and TCWV and Q_{net} is also robust, consistent with Figs. 9c and 9e. Although the impact of TCWV on the cool skin size does exist, yet it is minor compared to the effects of calmer winds and larger T_a-T_s. In addition, such warm waters and calm winds, together with the usually high solar insolation in this region, are manifestation of strong diurnal warming events. However, the residual diurnal warming at ~ 10 pm local time, if existing, would have resulted in a warmer skin (compared to the water at drifting or moored buoy depths, 0.2-1 m), rather than contributing to a cooler skin.

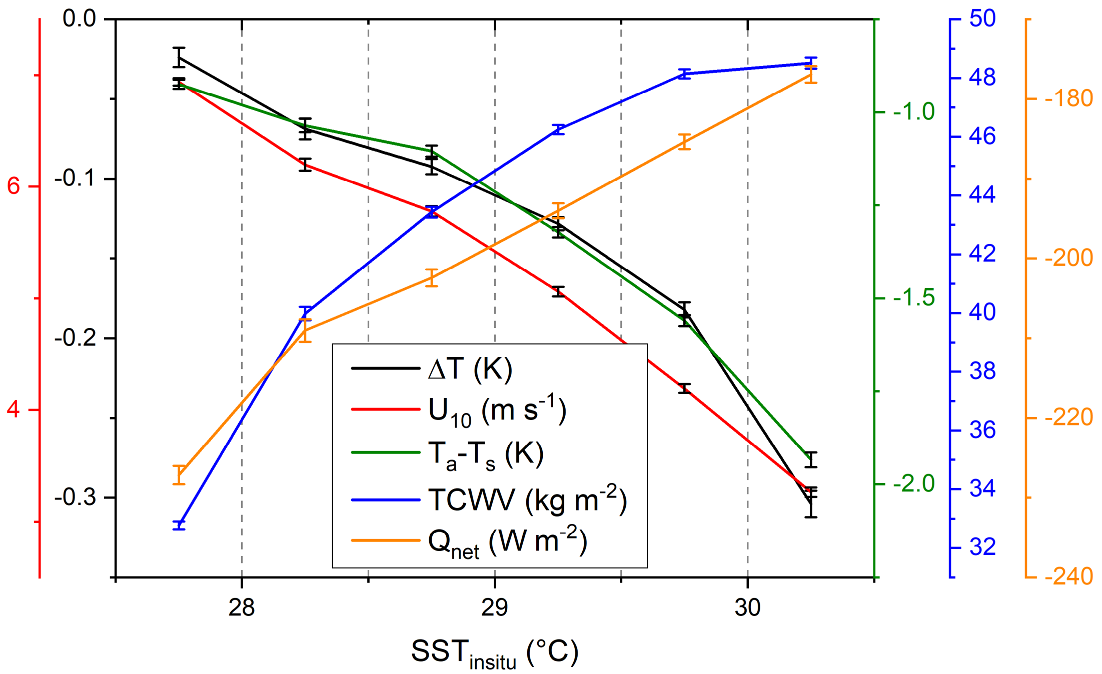

Fig. 10. Change of ΔT (black), U_{10} (red), T_a-T_s (green), TCWV (blue), and Q_{net} (brown), against SST_{insitu} over the tropical Indian Ocean and the TWP domain (50°E-180°, 20°S-20°N; see the white box in Fig. 9b). SST_{insitu} are divided into six bands: < 28 °C, every half a degree from 28 °C to 30 °C, and > 30 °C. The error bar indicates the 95% confidence level MoE.

4.4. Seasonal patterns of ΔT

The time series of monthly ΔT and SDs are shown in Fig. 11, both globally and separately for two hemispheres. Over the years, global average ΔT basically stays stable between -0.10 to -0.17 K with variations. The stronger fluctuations in early years are probably due to fewer collocations. Global ΔTs largely follow those of the northern hemisphere, due to its larger collocation contribution (Fig. 2b). A seasonal pattern can be easily recognized for most of the years for the southern hemisphere, with larger ΔT sizes in austral summer (and smaller in austral winter). The seasonal pattern in the northern hemisphere is less regular (except for year 2010). The SDs also keep steady over the years, but display a clear seasonal pattern, especially in the northern hemisphere with larger SDs in summer (~ 0.4 K) and lower in winter (~ 0.3 K). The SDs in the southern hemisphere are much lower and more consistent being around 0.2-0.3 K and shows no clear seasonal pattern. It is interesting to note smaller SDs in the southern hemisphere, presumably due (at least partly) to the fewer *in situ* platforms, and collocations.

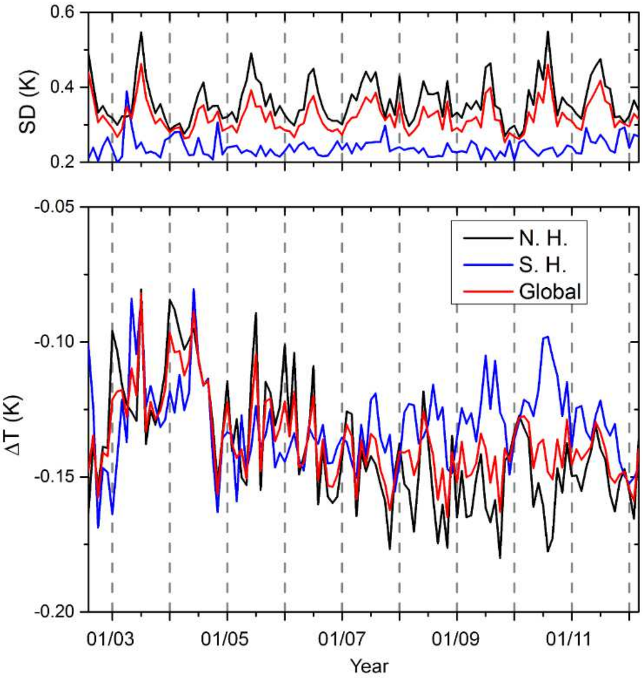

Fig. 11. Monthly time series of ΔT (bottom panel) and SDs (top panel) for the northern hemisphere (black line), southern hemisphere (blue line), and global coverage (red line).

Monthly mean, averaged over the whole study period, ΔT and environmental variables for both hemispheres are shown in Fig. 12. The seasonal pattern is more regular in the southern hemisphere with minimum ΔT size (~ -0.11 K) in austral winter and maximum (~ -0.14 K) in austral summer (Fig. 12a). The ΔT sizes in the northern hemisphere are larger in almost all the months, reaching ~ -0.16 K in August and -0.13 K in winter. Seasonal pattern of ΔT in the northern hemisphere is less regular (Fig. 12a). The meteorological variables show strong seasonal pattern in both hemispheres. The wind speeds in the northern hemisphere are smaller than those in the southern hemisphere for almost all months, largely accounting for the former's larger ΔT sizes (Fig. 12b). The minimum T_a-T_s in northern winter is lower (-2.2 K) than its counterpart in austral winter (-1.5 K), which also contributes to the larger ΔT in the northern hemisphere. In addition, the TCWV in the northern summer is higher than the maximum TCWV in the austral summer (~ 36 kg m^{-2} compared to ~29 kg m^{-2}), which may contribute to the irregularity of the seasonal pattern in the northern hemisphere.

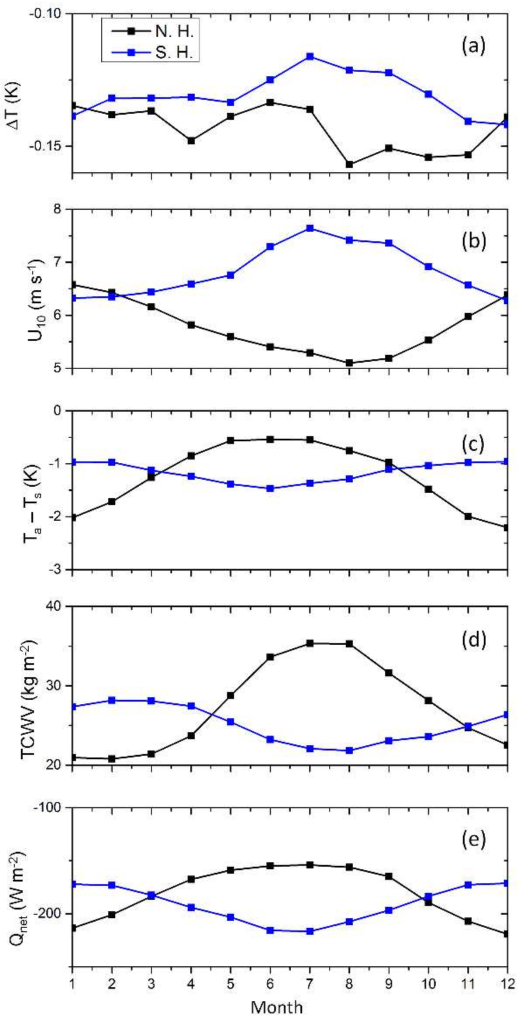

Fig. 12. Monthly mean (a) ΔT; (b) U_{10}; (c) T_a-T_s; (d) TCWV; and (e) Q_{net} for northern (black line) and southern (blue line) hemisphere.

5. Discussion

The AATSR dual-view three channel (D3) skin SST, in conjunction with high-quality *in situ* SSTs from the NOAA *i*Quam system, are employed here for cool skin analyses, thanks to its high quality (attributable to innovative sensor features, such as the dual-view geometry and stable calibration), and independency from *in situ* measurements (due to the physics-based retrieval algorithm). Several prior studies have touched on the cool skin effect using ATSRs data. For example, Murray et al. (2000) compared four-year ATSR SST_{skin} data with coincident bulk SSTs and found a night (~ 20.30 pm local time) cool skin amplitude of ~ -0.20 K, slightly larger than in this study. Horrocks et al. (2003) calculated nighttime cool skin as the difference between the ATSR-2 and *in situ* SSTs, to test the performance of a skin model. Only the cool skin change against wind speed was shown, and their corresponding D3 figure matches our result very well (cf. Fig. 12a in Horrocks et al., 2003). The general statistics shown in section 4.1 of this study, including the mean difference and low RSD between SST_{skin} and SST_{insitu} (Fig. 1a), and the spread pattern of ΔT (Fig. 1b), together with all the following analyses, consistently suggest that the AATSR D3 SST is well suited for skin SST studies. However, the temporal and spatial differences between satellite retrievals and *in situ* observations may be comparable to, or even larger than, those between SST_{skin} and SST_{depth}, which is the focus of this study. These factors, at least in part, may be responsible for the differences between results of this study, and the parameterizations (D02, M11, and A17 models) obtained from the collocated skin and depth data onboard the same ship.

The effect of dust on IR SST retrievals was minimized by applying the QL = 5 filter in AATSR data, which restricts the ATSRs Saharan Dust Index (ASDI) to a range of -0.2 to 0.2. ASDI is a new SDI proposed especially for the ATSRs, and it is available in each pixel. Although scaled to produce values comparable with visible aerosol optical depth (AOD), the ASDI differs from the AOD in that it may go negative, with values > ~ 0.2 presumably indicating the presence of dust (Good et al., 2012). Stricter ASDI filters, such as retaining data with ASDI from -0.15 to 0.15, have been also tested but no noticeable changes in the results were observed (not shown). Xu and Ignatov (2016) observed large negative differences between nighttime AATSR and *in situ* measurements over the regions such as to the west of tropical Africa and northern Indian Ocean. They argued that this may be due to the Saharan dust outbreaks or Indian aerosol over the Arabian Sea. Note that no dust filter was applied in their work, and findings in this paper should be much less sensitive to the effects of aerosols. For example, large cool skin amplitudes were observed in this study in the Gulf of Guinea, which is just slightly to the south of the areas under strong Saharan dust effects. Also, calm winds typically appear in such areas, which should be the major reason for the cool skin signals. In addition, Good et al. (2012) and Noyes et al. (2006) both showed evidence, suggesting that AATSR D3 data are robust to dust and aerosol effects; in fact, the dual view retrievals can be even slightly positively biased in the presence of Saharan dust. This gives us more confidence in the results obtained.

With regards to warm skins ($\Delta T > 0$ K), Minnett et al. (2011) argued that they may be "merely an artefact of the depth at which the bulk temperature measurements are taken". However, in this study, at least a large portion of the warm skin signals appears real. Warm skins account for 25.6% of all ΔT values, part of which may well correspond to the 14.0% case with positive T_a-T_s conditions. Considering a possible small warm bias in AATSR data, the residual diurnal warming effect (especially when U_{10} is < 2 m s^{-1}), and noises in both satellite and *in situ* measurements, the true percentage may very likely be < 25.6%. In the daytime, when solar insolation is present (not analysed in this study), it is expected that warm skin events may occur more frequently than at night, as the skin layer can absorb part of the solar insolation (e.g., Saunders, 1967; Fairall et al., 1996), and higher T_a may lead more positive T_a-T_s conditions. Nevertheless, more observations are required to validate this assumption, which may be subject of future work.

According to several previous cool skin models (e.g., Saunders, 1967), higher winds tend to result in much thinner cool skin layer depths, and hence in smaller ΔT amplitudes, regardless of stronger evaporation and heat loss. Since wind is closely coupled with waves and turbulent mixing coupled with wave breaking, one is naturally curious to explore possible links between cool skin and wave variables. As a preliminary check, we used one-year (2011) global wave data produced by running the third-generation spectral wave model WAVEWATCH III (hereafter WW3; WAVE-WATCH III Development Group, 2016). The observation-based physics of WW3 model are described in Rogers et al. (2012), Zieger et al. (2015), and Liu et al. (2019). The wave parameters selected in our analysis include: (1) significant wave height of the full wave spectrum, H_s; (2) significant wave height and peak wave length of the wind-sea partition, $H_{s,w}$ and $L_{p,w}$, from which wave steepness $\epsilon = \frac{1}{2}H_{s,w} \times 2\pi/L_{p,w}$; and (3) dominant wave breaking probability b_T. Among them, the H_s, $H_{s,w}$, and $L_{p,w}$ are formal output parameters of WW3. We calculated b_T based on the parameterization proposed in Babanin et al. (2001), given as:

$$b_T = 85.1[(\epsilon_p - 0.055)(1 + H_{s,w}/d)]^{2.33}$$

where d is the water depth, $\epsilon_p = 2k_p[\int_{0.7f_p}^{1.3f_p} F_w(f)df]^{1/2}$ is the significant steepness of the spectral peak, $F_w(f)$ is the frequency spectrum of the wind sea after filtration of swell, k_p and f_p are the peak wavenumber and frequency of $F_w(f)$, respectively. The reason why we are running WW3 offline, instead of using wave parameters available in the ERAI reanalysis dataset, is that the unique b_T parameter, estimated from the full wave spectra, is not included in the ERAI. Moreover, our parameterizations for the spectral wave model includes a wave breaking term (which incorporates both the inherent (saturation-based) breaking and cumulative breaking mechanisms; Babanin et al., 2010), a separate swell dissipation term based on the wave-induced turbulence theory (Babanin, 2011), as well as a nonlinear wind input term formularized from field observations (Donelan et al., 2006). Overall, this updated formulation is deemed to better capture the physical mechanisms involved. Wave parameters (e.g., H_s) based on this set of wave physics, have proved more accurate than the ERAI wave product (e.g., Ardhuin et al., 2010; Liu et al., 2019).

The results are shown in Fig. 13. Expectedly, ΔT amplitude decreases as H_S increases, since the H_S is typically an exponential function of wind speed, which also explains the climbing pattern of ΔT when H_S grows from 0 to 3 m (Fig. 13a). The function of ϵ is similar to that of U_{10}, although the trend is less regular due probably to a small collocation number and the further dependency of ϵ on wave lengths (Fig. 13b). Finally, b_T is a direct function of wave steepness (according to Babanin et al. (2011), the threshold of ϵ above which waves start to break is 0.055/0.9 = 0.061, as indicated in Fig. 13b) in the open deep oceans, rather than of U_{10}. Breaking waves only account for a very small proportion of all waves. Of all b_T values, 84.7% are zero and discarded. Only the positive b_T values (15.3%) are retained. Fig. 13c indicates that there is no clear dependency of ΔT on the b_T, which is consistent with the trend to the right of the ϵ = 0.061 threshold line in Fig. 13b. Since ΔT is already closely approaching the asymptotic value (~-0.09 K to -0.12 K) when ϵ is > 0.061, i.e. waves start to break, there is not much room left for the ΔT to change due to different b_T conditions. In the future, with more data available, further analyses such as the one considered here, could be of use to both SST and wave communities in terms of better understanding the skin effect, and further understand its link with the upper mixing investigation.

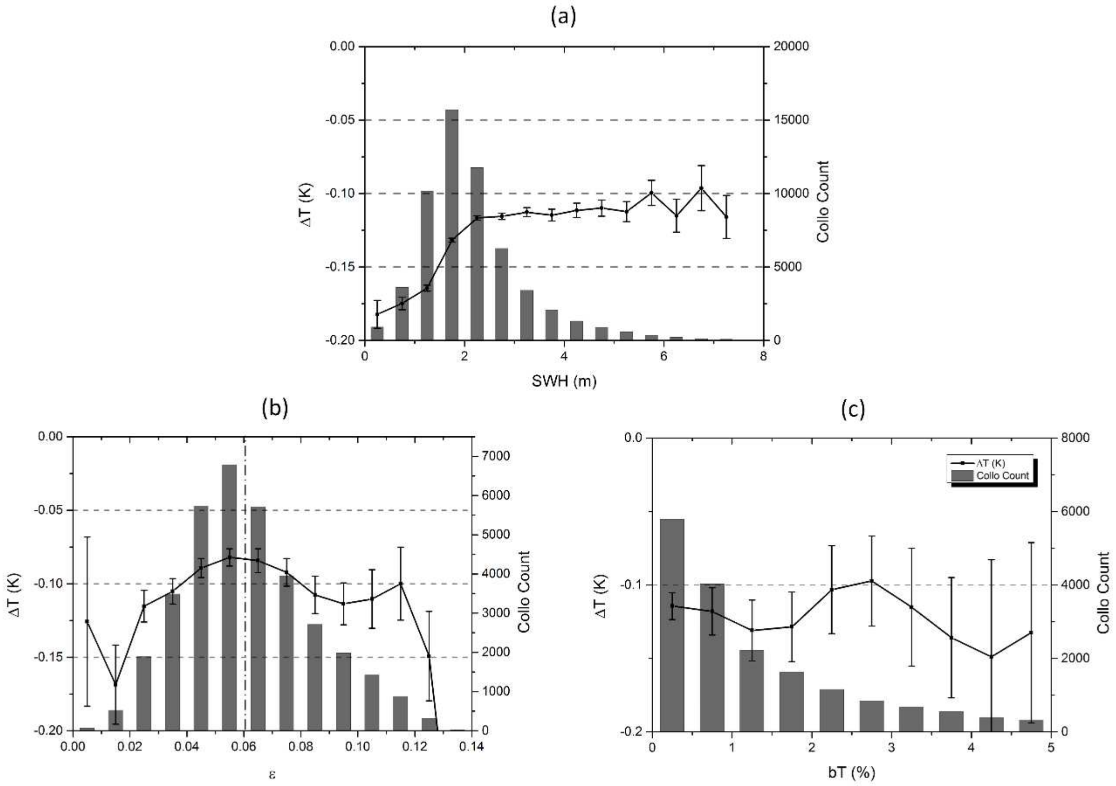

Fig. 13. The dependency of ΔT on (a) SWH, H_s, (b) wave steepness, ϵ, and (c) wave breaking probability (b_T in %). In panel (b), the wave breaking threshold of $\epsilon = 0.061$ is indicated. In panel (c), only b_T > 0% (accounting for 15.3% of all values) are retained. In all panels, black line is ΔT and error bar is the 95% confidence level MoE. Note all Y-axis ranges are only -0.2 K to 0 K.

6. Conclusions

Cool skin signals revealed from nighttime AATSR skin SST data and NOAA *i*Quam *in situ* SST measurements (defined as $\Delta T = SST_{skin} - SST_{insitu}$), have been described in detail on a global scale for nearly ten years from July 2002 to April 2012. Foci are on skin effects' overall statistics, dependencies on different meteorological variables, spatial distribution, and seasonal patterns. So far, the cool skin has not been systematically analysed on a global scale and over a long period, using a combination of high-quality satellite and *in situ* SST data. Traditional works in this area usually take advantage of the high accuracy shipborne radiometer SST_{skin} data and coincident SST_{depth}, which may have more accurate data but are inevitably limited to the ship's routes and duration.

In terms of dependencies of ΔT on environmental variables, wind speed is confirmed to play the most important role in the cool skin development, consistent with the findings in previous studies. The effect of T_a-T_s on the ΔTs is also significant. When the air is warmer than the sea, there can be warm skins. A small(er) variation range of T_a-T_s may be why its effect on ΔT appears secondary to that of U_{10}. The dependency of ΔT on TCWV is relatively weak. No clear dependency of ΔT on SST_{insitu} is observed for SST_{insitu} < 28 °C, above which, however, a dramatic increase of ΔT size is observed. The (partial) effect Q_{net} on ΔT turns out to be mild, since Q_{net} is largely coupled with U_{10}. A strong (moderate) dependency of ΔT on wave height (wave steepness) is identified in this study, while the correlation between ΔT and wave breaking probability is less discernible.

Spatially, large ΔT is normally associated with low U_{10}, yet other meteorological variables may or may not contribute. Typically, a combination of weak winds with large negative T_a-T_s and dry air profile, can lead to very cool skin, for instance over the Mediterranean Sea. The effects of different variables can sometimes offset (or amplify) each other. The spatial distributions of the correlation coefficients between ΔT and environmental variables further illustrate the more important effects of U_{10} and T_a-T_s. The tropical waters such as the tropical Indian Ocean and the TWP region have stood out. The cool skin amplitude gets significantly larger when SST_{insitu} increases from 28 °C to > 30 °C, especially when observed in conjunction with a sharp drop in U_{10} and T_a-T_s. The near 1 sensitivity of AATSR D3 data to actual SST and the data's near-independency on TCWV over this region, add to our confidence in the results.

The seasonal pattern of ΔT is more identifiable in the southern hemisphere with larger (smaller) average ΔTs in austral summer (winter), which is basically controlled by the wind speed pattern. In the northern hemisphere, ΔTs are larger than those in the southern hemisphere in all months, due to weaker winds. Also, ΔT in the northern hemisphere has a less regular seasonal pattern.

The spatial distribution and seasonal patterns of the cool skin can be useful in cool skin modelling as they may be part of the reason why many cool skin models, developed from seasonally and spatially different experiments, behave inconsistently with each other and some may seem less satisfying when intercompared together (e.g., Kent et al., 1996; Castro et al., 2003; Horrocks et al., 2003; Tu and Tsuang, 2005).

In the future, it may be worthwhile to explore combined ARC AATSR with microwave (MW) subskin SSTs (instead of *in situ* SSTs), to see if similar results can be obtained. Significantly larger collocation counts can be expected from two satellite products, to achieve improved statistical representativity and robustness. However, that would require highly accurate MW SSTs, which presently are challenging to obtain. For instance, Castro et al. (2008) tried to extract cool skin effect from AVHRR (Advanced Very High Resolution Radiometer) IR skin SST produced by Pathfinder project, and Tropical Rainfall Mapping Mission (TRMM) Microwave Imager (TMI) MW subskin SST retrievals. Although the dependency of the IR-MW differences on wind speed they obtained was consistent with the cool skin effect feature, they concluded that physical analyses of the skin layer process were strongly obscured by retrieval errors in both AVHRR IR and TMI MW SSTs. However, with AATSR SST_{skin} data and possibly more sophisticated MW sensors and/or retrieval algorithms (e.g., Nielsen-Englyst et al., 2018), it may be worth revisiting.

Acknowledgements

This work was supported by the Australian Research Council Discovery under Project DP170101328. The work of A. V. Babanin was supported by the DISI Australia-China Centre under Grant ACSRF48199. We would like to thank Helen Beggs and Chris Griffin for their useful comments on the manuscript. The views, opinions, and findings contained in this paper are those of the authors and should not be construed as an official NOAA or U.S. Government position, policy, or decision.

References

Akella, S., Todling, R., & Suarez, M. (2017). Assimilation for skin SST in the NASA GEOS atmospheric data assimilation system. *Quarterly Journal of the Royal Meteorological Society, 143*, 1032-1046. doi:10.1002/qj.2988

Alappattu, D.P., Wang, Q., Yamaguchi, R., Lind, R.J., Reynolds, M., & Christman, A.J. (2017). Warm layer and cool skin corrections for bulk water temperature measurements for air-sea interaction studies. *Journal of Geophysical Research: Oceans, 122*, 6470-6481. doi:10.1002/2017JC012688

Ardhuin, F., Rogers, E., Babanin, A.V., Filipot, J.-F., Magne, R., Roland, A., Van Der Westhuysen, A., Queffeulou, P., Lefevre, J.-M., & Aouf, L. (2010). Semiempirical dissipation source functions for ocean waves. Part I: Definition, calibration, and validation. *Journal of Physical Oceanography, 40*, 1917-1941. doi:10.1175/2010JPO4324.1

Artale, V., Iudicone, D., Santoleri, R., Rupolo, V., Marullo, S., & D'Ortenzio, F. (2002). Role of surface fluxes in ocean general circulation models using satellite sea surface temperature: Validation of and sensitivity to the forcing frequency of the Mediterranean thermohaline circulation. *Journal of Geophysical Research: Oceans, 107*(C8). doi:10.1029/2000JC000452

Babanin, A. V. (2011). Breaking and dissipation of ocean surface waves. Cambridge University Press, 480 pp., doi:10.1017/CBO9780511736162.

Babanin, A. V., Tsagareli, K. N., Young, I. R., & Walker, D. J. (2010). Numerical Investigation of Spectral Evolution of Wind Waves. Part II: Dissipation Term and Evolution Tests. *Journal of Physical Oceanography, 40 (4),* 667-683. doi:10.1175/2009JPO4370.1.

Babanin, A. V., Young, I. R., & Banner, M. L. (2001). Breaking probabilities for dominant surface waves on water of finite constant depth. *Journal of Geophysical Research: Oceans*, *106*(C6), 11659-11676. doi:10.1029/2000JC000215.

Brunke, M. A., Wang, Z., Zeng, X., Bosilovich, M., & Shie, C. (2011). An Assessment of the Uncertainties in Ocean Surface Turbulent Fluxes in 11 Reanalysis, Satellite-Derived, and Combined Global Datasets. *Journal of Climate, 24*, 5469–5493. doi:10.1175/2011JCLI4223.1

Brunke, M. A., Zeng, X., Misra, V., & Beljaars, A. (2008). Integration of a prognostic sea surface skin temperature scheme into weather and climate models. *Journal of Geophysical Research: Atmospheres, 113*(D21). doi:10.1029/2008JD010607

Brutsaert, W. (1975). A theory for local evaporation (or heat transfer) from rough and smooth surfaces at ground level. *Water Resources Research, 11*(4), 543-550. doi:10.1029/WR011i004p00543

Castro, S. L., Wick, G. A., & Emery, W. J. (2003). Further refinements to models for the bulk-skin sea surface temperature difference. *Journal of Geophysical Research: Oceans, 108*(C12). doi:10.1029/2002JC001641

Castro, S. L., Wick, G. A., Jackson, D. L., & Emery, W. J. (2008). Error characterization of infrared and microwave satellite sea surface temperature products for merging and analysis. *Journal of Geophysical Research: Oceans, 113*(C3). doi:10.1029/2006JC003829

Chaudhuri, A. H., Ponte, R. M., Forget, G., & Heimbach, P. (2013). A Comparison of Atmospheric Reanalysis Surface Products over the Ocean and Implications for Uncertainties in Air–Sea Boundary Forcing. *Journal of Climate, 26*, 153–170. doi:10.1175/JCLI-D-12-00090.1

Clayson, C. A., & Bogdanoff, A. S. (2013). The effect of diurnal sea surface temperature warming on climatological air–sea fluxes. *Journal of Climate, 26*(8), 2546-2556. doi:10.1175/JCLI-D-12-00062.1

Corlett, G., Barton, I., Donlon, C., Edwards, M., Good, S., Horrocks, L., . . . Nightingale, T. (2006). The accuracy of SST retrievals from AATSR: An initial assessment through geophysical validation against *in situ* radiometers, buoys and other SST data sets. *Advances in Space Research, 37*(4), 764-769. doi:10.1016/j.asr.2005.09.037

Dee, D. P., Uppala, S. M., Simmons, A., Berrisford, P., Poli, P., Kobayashi, S., . . . Bauer, d. P. (2011). The ERA-Interim reanalysis: Configuration and performance of the data assimilation system. *Quarterly Journal of the Royal Meteorological Society, 137*(656), 553-597. doi:10.1002/qj.828

Donelan, M. A., Babanin, A. V., Young, I. R., & Banner, M. L. (2006). Wave-Follower Field Measurements of the Wind-Input Spectral Function. Part II: Parameterization of the Wind Input. *Journal of Physical Oceanography, 36* (8), 1672-1689. doi:10.1175/JPO2933.1.

Donlon, C. J., Martin, M., Stark, J., Roberts-Jones, J., Fiedler, E., & Wimmer, W. (2012). The operational sea surface temperature and sea ice analysis (OSTIA) system. *Remote Sensing of Environment*, *116*, 140-158. doi:10.1016/j.rse.2010.10.017

Donlon, C., Minnett, P., Gentemann, C., Nightingale, T., Barton, I., Ward, B., & Murray, M. (2002). Toward improved validation of satellite sea surface skin temperature measurements for climate research. *Journal of Climate, 15*(4), 353-369. doi:https://doi.org/10.1175/1520-0442(2002)015<0353:TIVOSS>2.0.CO;2

Donlon, C., Robinson, I., Casey, K., Vazquez-Cuervo, J., Armstrong, E., Arino, O., . . . Piollé, J. (2007). The global ocean data assimilation experiment high-resolution sea surface temperature pilot project. *Bulletin of the American Meteorological Society, 88*(8), 1197-1214. doi:10.1175/BAMS-88-8-1197

Donlon, C. J., & Robinson, I. S. (1997). Observations of the oceanic thermal skin in the Atlantic Ocean. *Journal of Geophysical Research: Oceans, 102*(C8), 18585-18606. doi:10.1029/97JC00468

Embury, O., & Merchant, C. J. (2012). A reprocessing for climate of sea surface temperature from the along-track scanning radiometers: A new retrieval scheme. *Remote Sensing of Environment, 116*, 47-61. doi:10.1016/j.rse.2010.11.020

Embury, O., Merchant, C. J., & Corlett, G. K. (2012a). A reprocessing for climate of sea surface temperature from the along-track scanning radiometers: Initial validation, accounting for skin and diurnal variability effects. *Remote Sensing of Environment, 116*, 62-78. doi:10.1016/j.rse.2011.02.028

Embury, O., Merchant, C. J., & Filipiak, M. J. (2012b). A reprocessing for climate of sea surface temperature from the along-track scanning radiometers: Basis in radiative transfer. *Remote Sensing of Environment, 116*, 32-46. doi:10.1016/j.rse.2010.10.016

Fairall, C., Bradley, E. F., Godfrey, J., Wick, G., Edson, J. B., & Young, G. (1996). Cool-skin and warm-layer effects on sea surface temperature. *Journal of Geophysical Research: Oceans, 101*(C1), 1295-1308. doi:10.1029/95JC03190

Gentemann, C. L., Donlon, C. J., Stuart-Menteth, A., & Wentz, F. J. (2003). Diurnal signals in satellite sea surface temperature measurements. *Geophysical Research Letters, 30*(3). doi:10.1029/2002GL016291

Gentemann, C. L. & Minnett, P. J. (2008). Radiometric measurements of ocean surface thermal variability, *Journal of Geophysical Research: Oceans, 113*, C08017. doi:10.1029/2007JC004540.

Good, E., Kong, X., Embury, O., Merchant, C., & Remedios, J. (2012). An infrared desert dust index for the Along-Track Scanning Radiometers. *Remote Sensing of Environment, 116*, 159-176. doi:10.1016/j.rse.2010.06.016

Hasse, L. (1971). The sea surface temperature deviation and the heat flow at the sea-air interface. *Boundary-Layer Meteorology, 1*(3), 368-379. doi:10.1007/BF02186037

Hepplewhite, C. (1989). Remote observation of the sea surface and atmosphere The oceanic skin effect. *International Journal of Remote Sensing, 10*(4-5), 801-810. doi:10.1080/01431168908903920

Horrocks, L. A., Candy, B., Nightingale, T. J., Saunders, R. W., O'Carroll, A., & Harris, A. R. (2003). Parameterizations of the ocean skin effect and implications for satellite-based measurement of sea-surface temperature. *Journal of Geophysical Research: Oceans, 108*(C3). doi:10.1029/2002JC001503

Kennedy, J., Smith, R., & Rayner, N. (2012). Using AATSR data to assess the quality of *in situ* sea-surface temperature observations for climate studies. *Remote Sensing of Environment, 116*, 79-92. doi:10.1016/j.rse.2010.11.021

Kent, E. C., Forrester, T. N., & Taylor, P. K. (1996). A comparison of oceanic skin effect parameterizations using shipborne radiometer data. *Journal of Geophysical Research: Oceans, 101*(C7), 16649-16666. doi:10.1029/96JC01054

Kilpatrick, K., Podestá, G., Walsh, S., Williams, E., Halliwell, V., Szczodrak, M., . . . Evans, R. (2015). A decade of sea surface temperature from MODIS. *Remote Sensing of Environment, 165*, 27-41. doi:10.1016/j.rse.2015.04.023

Liu, Q., Erick Rogers, W., Babanin, A.V., Young, I.R., Romero, L., Zieger, S., Qiao, F., & Guan, C. (2019). Observation-based source terms in the third-generation wave model WAVEWATCH III: updates and verification. *Journal of Physical Oceanography, 49 (2),* 489-517. doi:10.1175/JPO-D-18-0137.1

Liu, W. T., Katsaros, K. B., & Businger, J. A. (1979). Bulk parameterization of air-sea exchanges of heat and water vapor including the molecular constraints at the interface. *Journal of the Atmospheric Sciences, 36*(9), 1722-1735. doi:https://doi.org/10.1175/1520-0469(1979)036<1722:BPOASE>2.0.CO;2

Llewellyn-Jones, D., Edwards, M., Mutlow, C., Birks, A., Barton, I., & Tait, H. (2001). AATSR: Global-change and surface-temperature measurements from Envisat. In *ESA bulletin* (Vol. 105, pp. 25).

Llewellyn-Jones, D., & Remedios, J. (2012). The Advanced Along Track Scanning Radiometer (AATSR) and its predecessors ATSR-1 and ATSR-2: An introduction to the special issue. *Remote Sensing of Environment*, 1-3. doi:10.1016/j.rse.2011.06.002

Masson, S., Terray, P., Madec, G., Luo, J.-J., Yamagata, T., & Takahashi, K. (2012). Impact of intra-daily SST variability on ENSO characteristics in a coupled model. *Climate dynamics, 39*(3-4), 681-707. doi:10.1007/s00382-011-1247-2

Matthews, A.J., Baranowski, D.B., Heywood, K.J., Flatau, P.J., & Schmidtko, S. (2014). The surface diurnal warm layer in the Indian Ocean during CINDY/DYNAMO. *Journal of Climate, 27*, 9101-9122. doi:10.1175/JCLI-D-14-00222.1

Merchant, C., Harris, A., Murray, M., & Závody, A. (1999). Toward the elimination of bias in satellite retrievals of sea surface temperature: 1. Theory, modeling and interalgorithm comparison. *Journal of Geophysical Research: Oceans, 104*(C10), 23565-23578. doi:10.1029/1999JC900105

Merchant, C. J., Embury, O., Rayner, N. A., Berry, D. I., Corlett, G. K., Lean, K., . . . Remedios, J. J. (2012). A 20 year independent record of sea surface temperature for climate from Along-Track Scanning Radiometers. *Journal of Geophysical Research: Oceans, 117*(C12). doi:10.1029/2012JC008400

Merchant, C. J., Embury, O., Roberts-Jones, J., Fiedler, E., Bulgin, C. E., Corlett, G. K., . . . Morak-Bozzo, S. (2014). Sea surface temperature datasets for climate applications from Phase 1 of the European Space Agency Climate Change Initiative (SST CCI). *Geoscience Data Journal, 1*(2), 179-191. doi:10.1002/gdj3.20

Minnett, P. J. (2003). Radiometric measurements of the sea-surface skin temperature: The competing roles of the diurnal thermocline and the cool skin. *International Journal of Remote Sensing, 24*(24), 5033-5047. doi:10.1080/0143116031000095880

Minnett, P. J., Smith, M., & Ward, B. (2011). Measurements of the oceanic thermal skin effect. *Deep Sea Research Part II: Topical Studies in Oceanography, 58*(6), 861-868. doi:10.1016/j.dsr2.2010.10.024

Murray, M., Allen, M., Merchant, C., Harris, A., & Donlon, C. (2000). Direct observations of skin-bulk SST variability. *Geophysical Research Letters, 27*, 1171-1174. doi:10.1029/1999GL011133

Nielsen-Englyst, P., L Høyer, J., Toudal Pedersen, L., L Gentemann, C., Alerskans, E., Block, T., & Donlon, C. (2018). Optimal Estimation of Sea Surface Temperature from AMSR-E. *Remote Sensing, 10*(2), 229. doi:10.3390/rs10020229

Noyes, E., Minnett, P., Remedios, J., Corlett, G., Good, S., & Llewellyn-Jones, D. (2006). The accuracy of the AATSR sea surface temperatures in the Caribbean. *Remote Sensing of Environment, 101*(1), 38-51. doi:10.1016/j.rse.2005.11.011

O'Carroll, A. G., Eyre, J. R., & Saunders, R. W. (2008). Three-way error analysis between AATSR, AMSR-E, and *in situ* sea surface temperature observations. *Journal of Atmospheric and Oceanic Technology, 25*(7), 1197-1207. doi:10.1175/2007JTECHO542.1

O'Carroll, A., Watts, J., Horrocks, L., Saunders, R., & Rayner, N. (2006). Validation of the AATSR meteo product sea surface temperature. *Journal of Atmospheric and Oceanic Technology, 23*(5), 711-726. doi:10.1175/JTECH1876.1

Paulson, C., & Simpson, J. (1981). The temperature difference across the cool skin of the ocean. *Journal of Geophysical Research: Oceans, 86*(C11), 11044-11054. doi:10.1029/JC086iC11p11044

Reynolds, R. W., Gentemann, C. L., & Corlett, G. K. (2010). Evaluation of AATSR and TMI satellite SST data. *Journal of Climate, 23*(1), 152-165. doi:10.1175/2009JCLI3252.1

Robertson, J., & Watson, A. (1992). Thermal skin effect of the surface ocean and its implications for CO2 uptake. *Nature, 358*(6389), 738-740. doi:10.1038/358738a0

Robinson, I., Wells, N., & Charnock, H. (1984). The sea surface thermal boundary layer and its relevance to the measurement of sea surface temperature by airborne and spaceborne radiometers. *International Journal of Remote Sensing, 5*(1), 19-45. doi:10.1080/01431168408948787

Rogers, W. E., Babanin, A. V., & Wang, D. W. (2012). Observation-consistent input and whitecapping dissipation in a model for wind-generated surface waves: Description and simple calculations. *Journal of Atmospheric and Oceanic Technology*, *29*(9), 1329-1346. doi:10.1175/JTECH-D-11-00092.1.

Saunders, P. M. (1967). The temperature at the ocean-air interface. *Journal of the Atmospheric Sciences,* *24*(3), 269-273. doi:https://doi.org/10.1175/1520-0469(1967)024<0269:TTATOA>2.0.CO;2

Schlüssel, P., Emery, W. J., Grassl, H., & Mammen, T. (1990). On the bulk-skin temperature difference and its impact on satellite remote sensing of sea surface temperature. *Journal of Geophysical Research: Oceans, 95*(C8), 13341-13356. doi:10.1029/JC095iC08p13341

Soloviev, A. V., & Schlüssel, P. (1994). Parameterization of the cool skin of the ocean and of the air-ocean gas transfer on the basis of modeling surface renewal. *Journal of Physical Oceanography,* *24*(6), 1339-1346. doi:https://doi.org/10.1175/1520-0485(1994)024<1339:POTCSO>2.0.CO;2

Soloviev, A. V., & Schlüssel, P. (1996). Evolution of cool skin and direct air-sea gas transfer coefficient during daytime. *Boundary-Layer Meteorology,* *77*(1), 45-68. doi:10.1007/BF00121858

Tu, C. Y., & Tsuang, B. J. (2005). Cool-skin simulation by a one-column ocean model. *Geophysical Research Letters, 32*(22). doi:10.1029/2005GL024252

Ward, B. (2006). Near-surface ocean temperature. *Journal of Geophysical Research: Oceans, 111*(C2). doi:10.1029/2004JC002689

WAVEWATCH III Development Group (WW3DG). (2016). *User manual and system documentation of WAVEWATCH III version 5.16.* Environmental Modeling Center, Marine Modeling and Analysis Branch, National Centers for Environmental Prediction.

Wick, G. A., Emery, W. J., Kantha, L. H., & Schlüssel, P. (1996). The behavior of the bulk–skin sea surface temperature difference under varying wind speed and heat flux. *Journal of Physical Oceanography, 26*(10), 1969-1988. doi:https://doi.org/10.1175/1520-0485(1996)026<1969:TBOTBS>2.0.CO;2

Wick, G. A., & Jessup, A. T. (1998). Simulation of ocean skin temperature modulation by swell waves. *Journal of Geophysical Research: Oceans, 103*(C2), 3149-3161. doi:10.1029/97JC03199

Woodcock, A. H. (1941). Surface cooling and streaming in shallow fresh and salt waters. *Journal of Marine Research, 4*, 153-161.

Woodcock, A. H. (1947). Temperatures observed near the surface of a fresh-water pond at night. *Journal of Meteorology, 4*, 102-103.

Wu, J. (1985). On the cool skin of the ocean. *Boundary-Layer Meteorology, 31*(2), 203-207. doi:10.1007/BF00121179

Xu, F., & Ignatov, A. (2014). *In situ* SST quality monitor (*i*Quam). *Journal of Atmospheric and Oceanic Technology, 31*(1), 164-180. doi:https://doi.org/10.1175/JTECH-D-13-00121.1

Xu, F., & Ignatov, A. (2016). Error characterization in *i*Quam SSTs using triple collocations with satellite measurements. *Geophysical Research Letters, 43*(20), 10826-10834. doi:10.1002/2016GL070287

Zàvody, A., Mutlow, C., & Llewellyn-Jones, D. (1995). A radiative transfer model for sea surface temperature retrieval for the along-track scanning radiometer. *Journal of Geophysical Research: Oceans, 100*(C1), 937-952. doi:10.1029/94JC02170

Zeng, X., & Beljaars, A. (2005). A prognostic scheme of sea surface skin temperature for modeling and data assimilation. *Geophysical Research Letters, 32*, L14605. doi: 10.1029/2005GL023030

Zhang, H., Beggs, H., Majewski, L., Wang, X.H., & Kiss, A. (2016). Investigating sea surface temperature diurnal variation over the Tropical Warm Pool using MTSAT-1R data. *Remote Sensing of Environment, 183*, 1-12. doi:10.1016/j.rse.2016.05.002

Zhang, H., Beggs, H., Merchant, C. J., Wang, X. H., Majewski, L., Kiss, A. E., Rodríguez, J., Thorpe, L., Gentemann, C., & Brunke, M. (2018). Comparison of SST diurnal variation models over the Tropical Warm Pool region. *Journal of Geophysical Research: Oceans*, 123, 3467-3488. doi:10.1029/2017JC013517

Zhang, H., Reynolds, R.W., Lumpkin, R., Molinari, R., Arzayus, K., Johnson, M., & Smith, T.M. (2009). An Integrated Global Observing System For Sea Surface Temperature Using Satellites and in Situ Data: Research to Operations. *Bulletin of the American Meteorological Society, 90*, 31–38. doi:10.1175/2008BAMS2577.1

Zieger, S., Babanin, A. V., Rogers, W. E., & Young, I. R. (2015). Observation-based source terms in the third-generation wave model WAVEWATCH. *Ocean Modelling*, *96*, 2-25. doi:10.1016/j.ocemod.2015.07.014.

Figure captions:

Fig. 1. (a) Density of collocations as a function of SST_{insitu}, with overall statistics of ΔT (= SST_{skin} - SST_{insitu}) superimposed. (b) Frequency distribution of ΔTs.

Fig. 2. (a) Spatial distribution of the collocations. Bin size is 10°×10°. (b) Monthly collocation counts in the northern (black bars) and southern (blue bars) hemispheres.

Fig. 3. Solid circles/Black line: dependencies of ΔT on U_{10}. The error bar is the 95% confidence level margin of error (MoE), i.e. 1.96 times the SD divided by the square root of the collocation number. The column bars indicate the collocation counts falling within each 1 m s^{-1} U_{10} interval. The red, blue, and green lines have been calculated using the Donlon et al. (2002), Minnett et al. (2011), and Alappattu et al., (2017) empirical parameterizations, respectively.

Fig. 4. (a) Dependency of ΔT on T_a-T_s (with the error bars at 95% confidence level margin of error, MoE). (b) Dependency of ΔT on T_a-T_s (binned into 0.5 K) and U_{10} (binned into 1 m s^{-1}). Black contour lines indicate the corresponding collocation counts in each 1 m s^{-1} × 0.5 K bin. Only bins with collocation counts >= 20 are plotted.

Fig. 5. Same as in Fig. 4 but for the dependency of ΔT on TCWV (binned into 5 kg m^{-2}).

Fig. 6. Same as Fig. 4 but for the dependency of ΔT on SST_{insitu} (binned into 1 °C).

Fig. 7. Same as Fig. 4 but for the dependency of ΔT on Q_{net} (binned into 50 W m^{-2}).

Fig. 8. Spatial distributions of (a) ΔT; (b) U_{10}; (c) T_a-T_s; (d) TCWV; (e) SST_{insitu}; and (f) Q_{net} averaged over the whole study period. Box size is 10° by 10°.

Fig. 9. Correlation coefficients between ΔT and (a) U_{10}; (b) T_a-T_s; (c) TCWV; (d) SST_{insitu}; and (e) Q_{net}. The white box in panel (b) is within (50°E-180°, 20°S-20°N). See text for further illustration.

Fig. 10. Change of ΔT (black), U_{10} (red), T_a-T_s (green), TCWV (blue), and Q_{net} (brown), against SST_{insitu} over the tropical Indian Ocean and the TWP domain (50°E-180°, 20°S-20°N; see the white

box in Fig. 9b). SST_{insitu} are divided into six bands: < 28 °C, every half a degree from 28 °C to 30 °C, and > 30 °C. The error bar indicates the 95% confidence level MoE.

Fig. 11. Monthly time series of ΔT (bottom panel) and SDs (top panel) for the northern hemisphere (black line), southern hemisphere (blue line), and global coverage (red line).

Fig. 12. Monthly mean (a) ΔT; (b) U_{10}; (c) T_a-T_s; (d) TCWV; and (e) Q_{net} for northern (black line) and southern (blue line) hemisphere.

Fig. 13. The dependency of ΔT on (a) SWH, H_s, (b) wave steepness, ϵ, and (c) wave breaking probability (b_T in %). In panel (b), the wave breaking threshold of $\epsilon = 0.061$ is indicated. In panel (c), only b_T > 0% (accounting for 15.3% of all values) are retained. In all panels, black line is ΔT and error bar is the 95% confidence level MoE. Note all Y-axis ranges are only -0.2 K to 0 K.